Quantum states of interacting electrons in a real quantum dot

N. A. Bruce and P. A. Maksym
Department of Physics and Astronomy, University of Leicester, Leicester LE1 7RH, United Kingdom
(Received 17 August 1999)

We present an exact diagonalization method that allows the electronic states of interacting electrons in a quantum dot to be calculated from first principles, without making assumptions about the shape of the confining potential, the dimensionality of the problem or the exact nature of the electronic states. The electrostatic potential of the entire device is calculated and the subband structure determined numerically to allow the full three-dimensional electron motion to be included in the calculation. Exact diagonalization of the many-body Hamiltonian then determines the states of the electrons in the dot within the effective-mass approximation. The screening due to the gate electrodes is also taken into account. This method may be used for a range of device geometries, but here we calculate the low-lying levels of a cylindrically symmetric, electrostatically confined quantum dot to better than 0.1%. Results for the ground-state energy and the far-infrared absorption spectrum are presented and the physical effects of the electron motion in the perpendicular direction and the screening are discussed.

I. INTRODUCTION

Semiconductor quantum dots are currently of immense interest as the possible use of dots in laser and electronic devices has provoked intense study of their properties. Theoretical studies of the physics of these systems have been based on a number of approximations, notably restriction of the system to two dimensions,[1,2] although some work has included three-dimensional electron motion.[3,4] There is increasing recognition that more detailed calculations are required to investigate particular device structures,[5] and this work is concerned with a general calculation technique that is free of the approximations and assumptions used in previous studies.

Most work on dots is based on a model in which the electron motion is two dimensional, the confining potential is parabolic and the electrons interact via the Coulomb interaction. Any model that includes more detail must account for the effect of the device structure that confines the electrons. The model should allow for the possibility of motion in all three dimensions, include a realistic confining potential that restricts the electron motion in each dimension and allow for the modifications to the interaction potential that occur in real systems, particularly those with metallic gates. This means that the electrostatic potential for the whole device must be calculated and included in the calculation of the electronic properties.

The procedure described here starts from a calculation of the electrostatic potential and leads to the quantum states of the interacting electron system from which electronic properties can be calculated. The general idea is to find a suitable single-particle basis from a combination of variational and Hartree-Fock approaches and use this basis to perform an exact diagonalization of the full Hamiltonian that includes realistic confinement and interaction potentials. This allows ground-state energies to be found to a numerical accuracy of better than 0.1% in a reasonable amount of computer time.

Although the primary aim of this work is to establish the viability and accuracy of our method, we also present some illustrative results for a structure that is typical of current devices. We look at the energy and angular momentum of the ground state and the dependence of these quantities on magnetic field. We compare these results with those for a two-dimensional (2D) system with similar characteristics and also with a model that does not take into account the screening due to the gate electrodes. In addition, we calculate the far-infrared absorption spectrum of the dot and identify effects that occur when the electron motion differs from the ideal 2D behavior. This allows us to make some general comments about the use of the 2D parabolic model for interpretation of experimental data.

The paper is organized as follows. We first present the specific device model that we use to illustrate our method and define the physics that we wish to include in calculations (Sec. II). Next, we detail our calculational procedures (Sec. III) and then present illustrative results and estimate the accuracy of our method (Sec. IV). Finally we summarize the main conclusions about our method and the effect of corrections to the 2D parabolic dot model. Appendixes give additional information about the matrix elements used for our calculations.

II. GENERAL PHYSICS OF A QUANTUM-DOT DEVICE

A. Device structure

Quantum-dot devices are often constructed from a heterojunction or quantum well that provides strong confinement in the vertical direction, creating a quasi-2D electron system. In order to further confine the electrons to form a quantum dot, confinement in the plane of the 2D system is required. This can be achieved in a number of ways. The most common is to use metallic gates in conjunction with an insulating cap in order to confine the electrons electrostatically.[6,7] However other methods are also employed, such as placing stressors on the surface of the device,[8] and dots can be fabricated directly by self-organized growth.[9]

We use a specific device to illustrate our method (Fig. 1), similar in style to many on which measurements have been

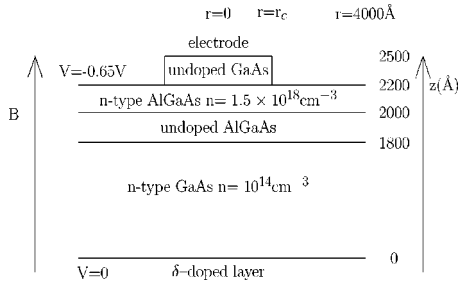

FIG. 1. Schematic cross section of the device structure used in the calculations.

made.[10] The device is made from the following layers. At the base of the device a drain electrode is constructed from a δ-doped layer of Si in GaAs. On top of this is an undoped layer of GaAs (1800 Å thick with donor density $n=10^{14}$ cm^{-3}), then a barrier layer of undoped $Al_xGa_{1-x}As$ (200 Å, $n=0$). The top full layer is of heavily doped n-type $Al_xGa_{1-x}As$ (200 Å, $n=1.5\times10^{18}$ cm^{-3}) and above this there is a circular cap of undoped GaAs (300 Å, $n=0$) with radius $r_c=2000$ Å. The top of the device (both the cap and the uncovered section of the preceding layer) is covered with a metal electrode. For simplicity, the ionized donor density is assumed to be uniform but it would be possible to include ionized donor density inhomogeneities.[11] The dielectric constants were chosen to be 12.4 for the GaAs and 11.8 for $Al_xGa_{1-x}As$, the g factor in GaAs was -0.44 and the Schottky offsets were 0.7 eV for GaAs and 0.95 eV for $Al_xGa_{1-x}As$. In all calculations we assume there are three electrons in the dot and we consider all possible spin polarizations. As we wish all the states we consider to be bound, we set the gate voltage at a level which ensures that the states have a negative energy with respect to that of electrons in the drain electrode. Therefore a gate voltage of -0.65 V was used. The conduction-band offsets due to the differing band gaps of the material were measured relative to the GaAs conduction-band edge. Thus the offset in the $Al_xGa_{1-x}As$ layers was taken to be 300 meV. All the results presented here are for this specific device, but we stress that our method is not limited to this device or even to devices with this general construction.

B. Hamiltonian

The Hamiltonian for electrons confined as described in Sec. II A is

$$H=\sum_i \frac{1}{2m^*}\{p_{\perp i}^2+(\mathbf{p}_{\parallel i}+e\mathbf{A})^2\}+U(\mathbf{R}_i)+V_I(\mathbf{R}_i)$$

$$+\tfrac{1}{2}\sum_{i\neq j} V(\mathbf{R}_i,\mathbf{R}_j)+g^*\mu_B BS_z. \qquad (1)$$

Here $\mathbf{A}$ is the magnetic vector potential, B is the magnetic field in the z direction, m^* and g^* are the electron effective mass and g factor, S_z is the z component of the total spin, and μ_B is the Bohr magneton. The subscripts $\parallel$ and $\perp$ denote components in and perpendicular to the (x,y) plane, respectively. U is the 3D confining potential, V_I is the interaction of each electron with its own image charge, and V is the electron-electron interaction potential. These terms are dependent on the 3D position $\mathbf{R}=(\mathbf{r},z)$ through the in-plane position $\mathbf{r}$ and z coordinate.

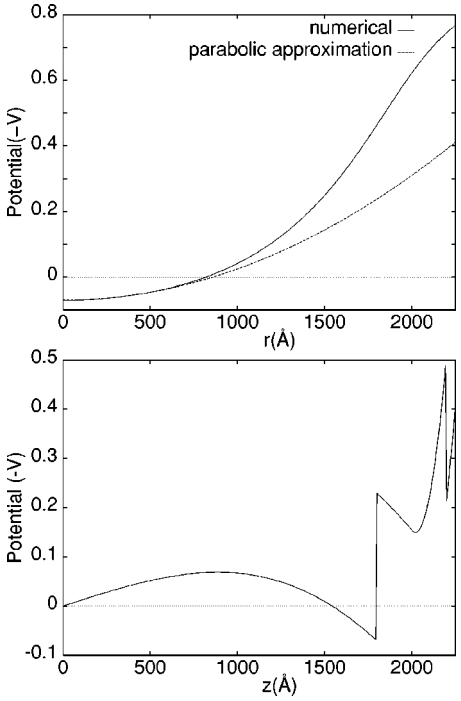

FIG. 2. Potential of the device in Fig. 1. The top panel shows the radial potential compared to a parabolic form with $\hbar\omega_0=4.65$ meV. The lower panel gives the conduction-band edge through the center of the device.

The confinement term, U is the 3D electrostatic potential in the device due to the gate electrodes and the impurities in the different materials. We calculate it by numerically solving the Poisson equation, whereas in 2D treatments it is generally approximated by a parabola. Figure 2 shows the numerically generated potential with the equivalent parabola superimposed. For radii less than 700 Å the parabolic approximation is very good. However, at larger radii the two curves diverge rapidly. This implies that for small angular momentum and large magnetic fields, the parabolic approximation holds well, but in general this may not be the case. The variation of the potential perpendicular to the plane, as shown in Fig. 2, is discontinuous and highly asymmetric.

As most of the devices we consider have metallic gates, we must take account of the screening of the Coulomb potential. The terms V and V_I are determined by applying the general approach of Hallam *et al.*[12] to the Poisson equation for charges in a gated device. The electron-electron potential V is simply related to the electrostatic Green's function, $G(\mathbf{R},\mathbf{R}')$, by $V(\mathbf{R},\mathbf{R}')=e^2G(\mathbf{R},\mathbf{R}')$, but a further step is required to obtain V_I. According to Ref. 12 the Green's function splits into two terms,

$$G(\mathbf{R},\mathbf{R}')=G_1(\mathbf{R},\mathbf{R}')+G_2(\mathbf{R},\mathbf{R}'), \qquad (2)$$

where G_1 is singular and results from a point charge at $\mathbf{R}'$. G_2 is a correction due to induced charges and V_I is obtained from this term by $V_I(\mathbf{R})=e^2G_2(\mathbf{R},\mathbf{R})/2$. For typical devices a cap structure provides a means to confine the electrons laterally. The cap is, in general, very much larger than the

average region of confinement of the electrons so it is reasonable to suppose that the screening can be well approximated with a parallel-plate capacitor treatment. This enables V and V_I to be obtained analytically from expressions given by Hallam *et al.*[12] (see also Sec. III C), which has the advantage of reducing computer time. Test calculations, described in Sec. IV C, confirm the accuracy of the parallel-plate capacitor approximation for a number of cases.

III. CALCULATIONAL METHOD

In this section we detail the method used to calculate the quantum states of interacting electrons in the dot. The second quantized form of the Hamiltonian is

$$H=\sum_{ij}\langle i|T_{\|}+T_{\perp}+U+V_I|j\rangle c_i^{\dagger}c_j+\tfrac{1}{2}\sum_{ijkl}\langle ij|V|kl\rangle c_i^{\dagger}c_j^{\dagger}c_k c_l + g^{*}\mu_B B_z S_z, \tag{3}$$

where $i, j, \ldots$ are single-particle states and $T_{\|}$ and $T_{\perp}$ denote kinetic energy operators, which include magnetic field effects. The eigenstates of this Hamiltonian are found by numerical diagonalization in a Slater determinant basis. A single-particle basis is needed to construct the many-particle basis and the choice of this basis is critical. We could of course choose any complete set as a basis, but an arbitrary choice would result in a large number of basis states being required to achieve good accuracy. This is because the states of a quantum dot are localized in space. Using a plane-wave basis set, for example, would require a very large number of Fourier components to define a localized state. To minimize the number of basis states required, and hence make the calculation tractable given finite computing resources, we attempt to choose a basis set that represents the physical system as closely as possible. In this way we reduce the total size of the Hamiltonian we need to diagonalize in order to obtain the energy levels of the system to an acceptable level of accuracy.

To construct the single-particle basis we choose functions that are separable into an in-plane (parallel to the interface) and a perpendicular part. The Fock-Darwin states are a good choice for the in-plane states because they are the eigenstates of parabolically confined electrons in a magnetic field, and the parabolic form is a good approximation sufficiently close to the minimum of the real potential. The perpendicular, or subband, functions are determined numerically by solving a one-dimensional Hartree-Fock equation: all the electrons are taken to be in the same subband and the energy of a single Slater determinant composed of products of Fock-Darwin states and subband states is minimized to obtain the subband states. Further details are given in Sec. III A.

After the single-particle basis has been found it is used to find the matrix elements in Eq. (3) and a standard exact diagonalization program is used to find the eigenstates of the electrons in the dot. The methods used for the matrix element calculation are given in the Appendixes and some details of the calculation of electrostatic potentials and Green's functions that appear in the matrix elements are given in Secs. III B and III C.

A. Single-particle basis

The basis functions are taken to have the form

$$\psi_i(\mathbf{R})=\chi_i(z)\phi_i(\mathbf{r}), \tag{4}$$

where the $\phi_i(\mathbf{r})$ are the in-plane functions and $\chi_i(z)$ are subband functions. The Fock-Darwin states[13] used for the in-plane basis have the form

$$\phi_{nl}(\mathbf{r})=N_{nl}r^{|l|}L_n^{|l|}\left(\frac{r^2}{2a^2}\right)e^{-r^2/4a^2}e^{-il\theta}, \tag{5}$$

where N_{nl} is the normalization constant, $L_n^{|l|}$ are associated Laguerre polynomials, and a is a length parameter. In the 2D noninteracting case $a^2=\hbar/(2m^*\Omega)$, where $\Omega=(\frac{1}{4}\omega_c^2+\omega_0^2)^{1/2}$, ω_0 is the in-plane confinement frequency, and $\omega_c=eB/m^*$ is the cyclotron frequency. The Fock-Darwin states are orthogonal for *any* value of a and we attempted to increase accuracy by treating this parameter as a variational parameter whose value was determined by the energy minimization procedure used to find the subbands.

To determine the subband states we suppose that all electrons are in the lowest subband and approximate the N-electron wave function Ψ as a Slater determinant composed of N states of the form $\chi(z_i)\phi_i(\mathbf{r}_i)$, where each electron has the same subband function. In principle, spin functions can be included in this Slater determinant but, as discussed in Sec. IV D, we have only used spin-polarized states. Minimizing the energy of the state Ψ subject to the constraint that $\chi(z)$ is normalized leads to a one-dimensional Schrödinger equation for $\chi(z)$. To perform the minimization we consider the quantity

$$\mathcal{A}=\langle\Psi|H|\Psi\rangle-\lambda\left\{\int\chi^{*}(z)\chi(z)dz-1\right\}, \tag{6}$$

where λ is a Lagrange multiplier. We now introduce a small change, $\delta\chi$ and denote the resulting change in Ψ by $\delta\Psi$. We find the first-order change in $\mathcal{A}$ is

$$\delta\mathcal{A}=\langle\delta\Psi|H|\Psi\rangle-\lambda\int\delta\chi^{*}(z)\chi(z)dz+\text{H.c.}, \tag{7}$$

where H.c. denotes Hermitean conjugate. $\mathcal{A}$ is stationary with respect to first-order variations in χ when $\delta\mathcal{A}$ vanishes and it follows that $\chi(z)$ is determined by the equation

$$\left[\frac{p_{\perp}^2}{2m^*}+\overline{U}(z)+V_{HF}(z)\right]\chi(z)=\epsilon(a)\chi(z). \tag{8}$$

Here $\epsilon(a)$ is a new variational parameter defined by the relation

$$\epsilon(a)=\frac{\lambda}{N}-\frac{1}{N}\sum_k\int\phi_k^{*}(\mathbf{r})\frac{(\mathbf{p}_{\|}+e\mathbf{A})^2}{2m^*}\phi_k(\mathbf{r})d\mathbf{r}, \tag{9}$$

where the sum runs over all electrons. The quantities $\overline{U}(z)$ and $V_{HF}(z)$ that appear in Eq. (8) are laterally averaged confinement and Hartree-Fock interaction potentials, respectively, which are given by the equations

$$\overline{U}(z)=\frac{1}{N}\sum_{k}\int \phi_k^*(\mathbf{r})U(z,\mathbf{r})\phi_k(\mathbf{r})d\mathbf{r}, \tag{10}$$

$$V_{HF}(z)=\frac{1}{N}\sum_{ij}\int \phi_i^*(\mathbf{r})\phi_j^*(\mathbf{r}')V(\mathbf{R},\mathbf{R}')[\phi_i(\mathbf{r}')\phi_j(\mathbf{r}) - \phi_j(\mathbf{r}')\phi_i(\mathbf{r})]|\chi(z')|^2 dz'd\mathbf{r}d\mathbf{r}'. \tag{11}$$

Equation (8) has the form of a single-particle Schrödinger equation. It can be solved numerically for any value of the variational parameter a and its solution gives a complete set of subband functions.

The value of a determines how accurate the results with the truncated basis set are. If a complete set of states was used as a basis, the value of a would be immaterial. However, we wish to use as small a number of states as possible. The value of a determines the radius of the in-plane states and initially we assumed that it would be advantageous to choose a to minimize the Hartree-Fock energy. It turned out, however, that the exact ground-state energy for the particular device considered here, is relatively insensitive to a provided that a reasonably realistic value is used. A detailed discussion of this point is given in Sec. IV D.

B. Electrostatic potential

The electrostatic potential U due to fixed charges and electrodes in the device, is found by solving the Poisson equation. The device has circular symmetry and the Poisson equation was solved on a 2D (400×400) grid. Boundary conditions were chosen such that the potential was fixed at the two electrodes and its radial derivative went to zero at the other boundaries. The radius of the structure was chosen to be 4000 Å as any increase in the radius had negligible effect on the potential of the active region. Thus finite-size effects are believed to be negligible. The potential was calculated at each grid point using a finite difference relaxation method that determines the potential iteratively, starting from zero potential at all internal grid points. The convergence criterion was that potential did not change by more than 0.1%, at any grid point, in successive iterations.

C. Screening

The parallel-plate capacitor form of the electrostatic Green's function is derived in Ref. 12. Results necessary for the present work are the Green's function itself and the nonsingular part G_2 that determines image charge effects. The Green's function is given by

$$G(\mathbf{R},\mathbf{R}')=\frac{1}{(2\pi)^2\varepsilon}\int\frac{f(k,z,z')}{k}e^{i\mathbf{k}\cdot(\mathbf{r}-\mathbf{r}')}d\mathbf{k} \tag{12}$$

where ε is the dielectric constant,

$$f(k,z,z')=\frac{\sinh[k(d-z)]\sinh(kz')}{\sinh(kd)} \tag{13}$$

for $z\leqslant z'$ and

$$f(k,z,z')=\frac{\sinh[k(d-z')]\sinh(kz)}{\sinh(kd)} \tag{14}$$

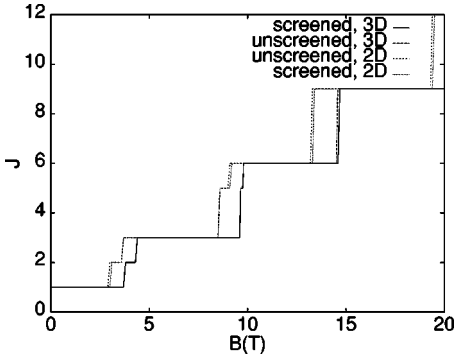

FIG. 3. Ground-state angular momentum as a function of applied magnetic field for 3D and 2D systems with screened and unscreened potentials.

otherwise. Here z and z' denote distances from the bottom plate and d is the plate separation. G_2 is given by

$$G_2(\mathbf{R},\mathbf{R})=\frac{1}{2\pi\varepsilon}\int_0^\infty dk\left[f(k,z,z)-\frac{1}{2}\right]. \tag{15}$$

IV. RESULTS

We begin with a brief overview of the physical effects of motion out of the plane and then present results. In addition to results for the ground state we look at the optical transitions of the system, the accuracy of the parallel-plate screening approximation and of our method in general.

Transitions of the angular momentum of the ground state as a function of magnetic field were predicted in early work on the 2D model for quantum dots.[1] These transitions occur when the increasing interaction energy due to the compression of the electron wave function by the magnetic field becomes large enough to make an increase in the radius of the states, and hence confinement energy, favorable. This also results in an increase of the total angular momentum of the system. The lowest-energy states at each magnetic field are known as magic number states as they correspond to a series of specific angular momentum values.

We can anticipate the general effect of including the motion perpendicular to the plane by using simple physical arguments. The main effect will be to allow the electrons to increase their separation and hence reduce their interaction energy, but retain about the same confinement energy. This will allow each magic number state to persist to a greater magnetic field before the increase of interaction energy causes a transition. We expect that the transitions between magic number states will therefore occur at higher fields in the 3D case than for the pure 2D case. A similar argument can be made for the screened interaction in comparison to the pure Coulomb interaction. Thus the screened system should again have transitions at higher fields than for the unscreened case.

A. Ground states

Transitions of the ground state for the device in Fig. 1 are presented in Fig. 3. The figure shows the ground-state angular momentum, calculated exactly, in comparison with results for an equivalent 2D model, with parabolic confine-

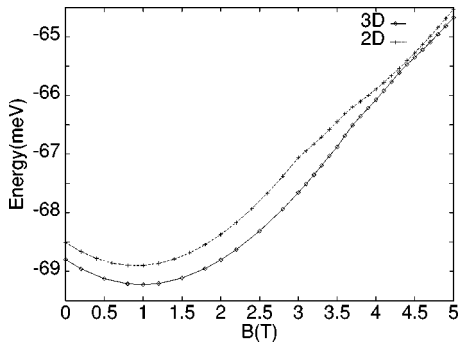

FIG. 4. Energy of the ground state as a function of magnetic field at low field for 3D and 2D screened cases. Points denote energies; lines are to guide the eye.

ment, for both screened and unscreened potentials. We can see immediately that all of the curves have a similar character. This shows that the 2D calculations do include all of the essential physics of the problem. However, the 2D model consistently has transitions at smaller magnetic fields, typically of the order of 10% too small. Additionally, it is interesting to note that unpolarized states continue to exist as the ground state up to 10 T, an effect that is more pronounced in the 2D case than for the more realistic model. Using a pure Coulomb potential, on the other hand, has very little effect on the angular momentum transitions of the ground state. This does *not* imply that screening is always unimportant. The dot plane is relatively far from the plates in the present case but a change in device geometry could increase the effect of screening.[14]

The energies of the ground states (Fig. 4) show that, again, the 2D and 3D results have a remarkably similar behavior. Note that in the figure the energy of the 2D curve has been offset by 121 meV so that a direct comparison can be made. The largest variation between the curves is due to the relative positions of the transitions. The energy gradient of the 2D curve is greater than that of the 3D curve. This again implies that the 2D curve will reach the transition condition at a lower magnetic field than that for the 3D case.

These results have important consequences for interpretation of experimental data. The shift in the transition field is of the order 1 T, and although this is not so large that the qualitative predictions of the 2D parabolic model are invalid, it is much too large for the model to be accurate. The only way to increase a transition field in the 2D parabolic model is to increase the strength of the confinement but the transition field is a slowly varying function $[\sim(\hbar\omega_0)^{1/3}]$ of the confinement energy.[15] There would be a considerable overestimate of the confinement energy if observed transitions were used to fit the confinement energy in the 2D parabolic model. For example, it would be necessary to double the confinement energy to obtain a shift of about 1 T in a transition occurring at a field of around 4 T in the 2D parabolic model. This factor is roughly consistent with a discrepancy in the confinement energies reported in recent experimental[16] and theoretical[17] work.

B. Optical transitions

Optical (far-infrared) experiments are, in general, insensitive to the number of electrons in a quantum dot. The reduced sensitivity is a consequence of the generalized Kohn's theorem,[1,18] which shows that electromagnetic radiation only affects the center of mass motion in a 2D dot with exact parabolic confinement. This leads to an excitation spectrum identical to that of a single particle but in reality, the observed spectrum has some small splittings. Some of these have been attributed to nonparabolic confinement,[19] but the additional effect of out-of-plane electron motion has not yet been considered. This can cause additional coupling of center of mass and relative motion and hence affect the excitation spectrum. Optical excitation can promote an electron to the next Landau level and there is, in general, a field range where the energy required for this transition is close to that required for a transition to a higher subband. It is at this point that the higher subbands are most likely to affect the optical spectrum.

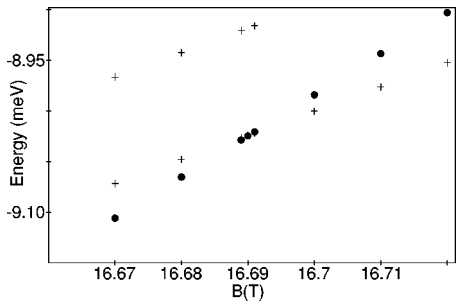

FIG. 5. Absorption spectrum for subband spacing of 27.14 meV. Point sizes are proportional to the total absorption for each level. Crosses denote points too small to be visible.

To investigate this we consider absorption of linearly polarized electromagnetic radiation. The transition rate from a single-electron state i to an excited state k is proportional to $|\langle k|x|i\rangle|^2$, where the electric field of the incident radiation is polarized in the x direction and $|i\rangle$ and $|k\rangle$ are initial and final states.[20] We use a similar expression in second quantised form to determine the relative strengths of the absorption lines for each many-body state. As a check on the accuracy of our results we use the f-sum rule,[20] which is satisfied to better than 1%.

We assess the importance of subband coupling by examining the optical absorption spectrum for several cases. The spectrum in the vicinity of $B=16.7$ T for the device described in Sec. II A is shown in Fig. 5. The crossing shown in the figure involves one state of predominantly first subband character and a second of predominantly second subband character. The sizes of the points in the figure give the relative transition rates to the states. Points marked with a + have transition rates at least two orders of magnitude less than those with dots. We can therefore see that there is very little chance of a transition to the upper subband state in this particular case. Very close to the crossing, the rate in the second subband state does rise by two orders of magnitude. However, this still gives a much smaller total rate than for the other state and so would still be very difficult to detect. The subband spacing in this case is about 27 meV and the behavior shown is probably typical for a large subband spacing.

To examine the possible behavior with a smaller subband spacing we artificially reduce the intersubband gap to 10 meV while retaining the form of the subband functions. This

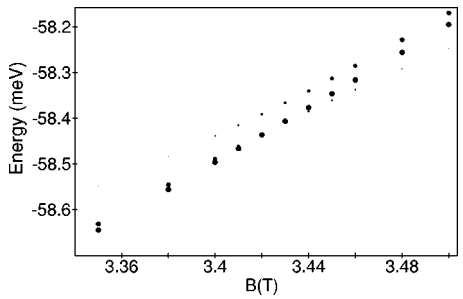

FIG. 6. Absorption spectrum for subband spacing of 10.0 meV. Point sizes are proportional to the total absorption for each level.

has the effect of reducing the energy spacing of the subbands but keeping their character unchanged. We now find evidence of both anticrossing and a significant transition rate to the upper subband state at $B=3.45$ T. Figure 6 shows the behavior of three states as they approach each other. The pair of states is mainly of first subband and the other state is of second subband character. We see that the lower state of the pair is unaffected by the presence of the upper subband level, whereas the other state shows strong anticrossing behavior. The selection of only one of the pair of states to be involved in anticrossing is physically reasonable and the mixing, hence repulsion, between levels occurs preferentially between levels which contain predominantly the same set of single particle angular momenta. These results indicate that subband coupling could cause electron-electron interactions to have an observable effect on the optical absorption spectrum for appropriate types of device.

C. Screening

In this section we consider exact results for the screening effect of the electrodes. We explain the numerical procedure for calculating the exact screened potential and we compare results of numerical and approximate calculations for a range of physical parameters and discuss the accuracy of the parallel-plate approximation.

The electrostatic Green's function that determines the exact interaction potential can be calculated numerically in a similar way to the electrostatic potential. However, G diverges at $\mathbf{R}=\mathbf{R}'$ and its behavior in this region is therefore unlikely to be accurately reproduced in a finite grid calculation. In order to obtain more reliable results we consider only the nonsingular part of the Green's function, F, defined by

$$G(\mathbf{R},\mathbf{R}')=\frac{1}{4\pi\varepsilon|\mathbf{R}-\mathbf{R}'|}+F(\mathbf{R},\mathbf{R}'). \tag{16}$$

We expect F to be well behaved over all space and also to be well represented on a finite grid. We therefore need to convert the equations for G into equations for F. The equation for G is

$$\nabla^2 G(\mathbf{R},\mathbf{R}')=-\frac{\delta(\mathbf{R}-\mathbf{R}')}{\varepsilon} \tag{17}$$

hence the equation for F is

$$\nabla^2 F(\mathbf{R},\mathbf{R}')=0, \tag{18}$$

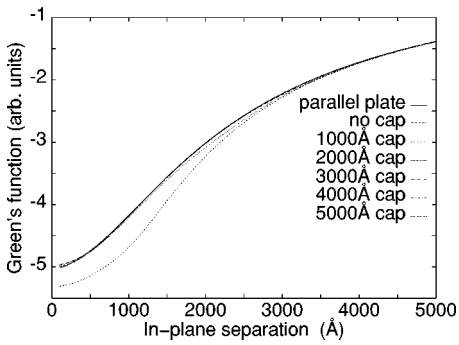

FIG. 7. Nonsingular part of the in-plane Green's function for the device in Fig. 1 with several cap sizes compared with the analytic result for an infinite parallel-plate capacitor.

and the boundary conditions for F are

$$G=0 \quad \text{at } z=0,d \Rightarrow F=-\frac{1}{4\pi\varepsilon|\mathbf{R}-\mathbf{R}'|},$$

$$\frac{\partial G}{\partial r}=0 \quad \text{at } r=0,r_{max} \Rightarrow \frac{\partial F}{\partial r}=\frac{r}{4\pi\varepsilon[r^2+(z-z')^2]^{3/2}}$$

together with

$$\varepsilon_1 \left.\frac{\partial F}{\partial z}\right|_{z_{0+}} = \varepsilon_2 \left.\frac{\partial F}{\partial z}\right|_{z_{0-}} \tag{19}$$

at any boundary, z_0, between materials 1 and 2.

To estimate the accuracy of the parallel-plate approximation, we compared numerical Green's functions with those calculated using Eq. (12). We varied the size of the cap (r_c) and the distance of the dot plane (given by the value of $z=z'$) from the plates for our test device. This enabled the robustness of the analytic form to be tested against variation from the ideal parallel-plate geometry. Results for $z=z'=d/2$ Å and $r'=0$ (Fig. 7) show that the exact in-plane Green's function differs from the parallel plate form by at most around 1% when the cap radius is 2000 Å or more and the in-plane separation is less than about 1000 Å. We also examined the out-of-plane Green's function ($z\neq z'$) for a reasonable range comparable to the size of the electron wave function in a dot and found agreement as good as that in Fig. 7. As the cap size increases, the agreement with the parallel-plate form gets better, as expected. The analytical expression Eq. (12) provides a good approximation for distances less than the cap radius. As the cap size of our device is 2000 Å, and the dot size is of the order of 500 Å, we use the analytic form in all calculations for our model device and anticipate it to be useful in most calculations using this method. However, we stress that our method can be adapted to use a numerical interaction potential, which may be necessary for more complicated geometries.

D. Accuracy of the method

In this section we detail the numerical accuracy of our calculation of the ground-state energies. We also discuss the numerical parameters which affect the calculation and describe their role. Initially we will address the issue of the

cutoff point for the basis set and estimate the errors inherent in using a finite basis. Then we consider the variational parameter a and its effect on the results.

To determine the number of single-particle basis states we examined the convergence with respect to the numbers of Landau levels and subband states at $B=0$, 7, and 20 T, field values which are far from ground state transitions. For $B=0$ T we found that using up to the third Landau level and a single subband was sufficient. Increasing the number of Landau levels by one shifted the ground-state energy by ≈ 0.03 meV, equivalent to an error of $\approx 0.05\%$. Similarly the addition of a second subband reduced the ground-state energy by ≈ 0.02 meV. For $B=7$ T the error due to the addition of an extra Landau level (≈ 0.008 meV) or subband (≈ 0.005 meV) was smaller than for the $B=0$ T case. This was expected as the predominant contribution to the error was from the limited number of Landau levels as the separation of the subbands was of the order of 27 meV, compared to a Landau-level spacing of approximately 4.65 meV at $B=0$ T and 7.63 meV at $B=7$ T. Similarly for $B=20$ T, including the third Landau level gave a change in the ground-state energy of only 0.001 meV and including a second subband, 0.002 meV. Note that at magnetic fields of this strength the Landau-level spacing (17.89 meV) is becoming comparable to the subband spacing (27.24 meV). This leads to errors of the same magnitude from truncating each part of the basis. These results imply that using a truncated basis of single-particle states up to the third Landau level and only the lowest subband give ground state energies with maximum errors of the order of 0.05% or 0.03 meV. This small amount of subband mixing is mainly due to the large energy spacing of the sub-bands. Note that not all nanostructures capable of being modelled using this method will have such strong confinement in the z direction. However, similar accuracies should be achievable in such cases by using an appropriately truncated basis set.

Another issue relevant to the numerical accuracy of the basis set is the magnetic field dependence of the subband basis. The variation of the ground subband wave function as a function of magnetic field was very small as shown in Fig. 8 (lower frame). The higher subbands had a greater variation with magnetic field (Fig. 8, upper frame), as did those calculated with a screened compared with an unscreened interaction potential. Due to the large energy spacing the calculations only required one or two subbands. This relative independence of field allowed the $B=0$ T subbands to be used in all calculations. Different subband sets were used for the screened and unscreened cases. Each of these was a complete set, so any errors due to this procedure are included in the variation of the ground state with the number of subbands in the basis set. As a guide, the energy of the ground state at $B=20$ T, calculated using $B=0$ T subband functions shifted by approximately 0.02 meV.

The value of a used for calculations is determined in a number of steps. First, we choose a magic number that we think will give the lowest-energy state. We know that the combination of single-particle states that gives the lowest energy is one that has consecutive angular momentum quantum numbers.[4,21] We assume that the transitions would occur at approximately the same fields and to the same states as in the 2D case.[1] We then calculate the energy of this state

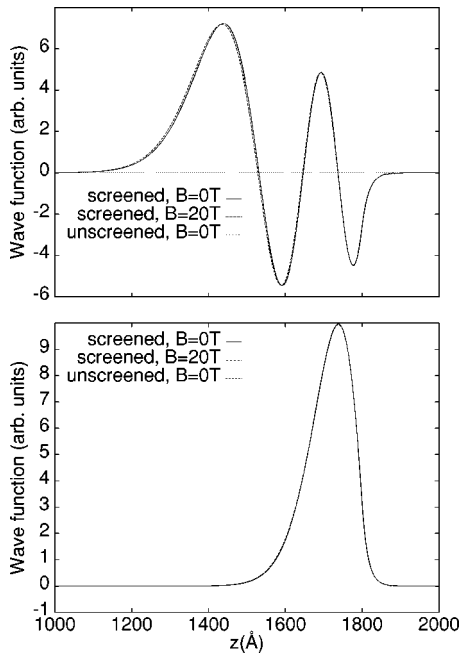

FIG. 8. Subband wave functions calculated with the Hartree-Fock procedure for a screened potential at $B=0$ and 20 T and an unscreened potential at $B=0$ T. The ground subband function is shown in the lower frame and the fourth subband function in the upper frame.

within the Hartree-Fock prescription as a function of a. The value of a that gives the lowest energy is then chosen for use in the rest of the calculation. Although the method used did not take full account of the possible spin states—a spin-polarized state was assumed—comparison with subbands calculated using the Hartree approximation gave no notable difference, thus implying that the form of the approximation in determining a is not important. For studies with larger numbers of electrons the same conclusions may not hold, but it would be possible to modify the procedure to account for spin variations. For fields close to the ground-state transitions, it is difficult to predict which angular momentum will give the minimum energy in the exact calculation. In the middle of the B range being considered ($B=9.8$ T) we looked at the variation of the optimum length parameter between the $J=3$ and $J=6$ states. The optimal values of a differed by 3%. The corresponding difference in the ground-state energy was less than 0.01%.

Finally, we examined the a dependence of the ground-state energy. We found that the ground-state energies for the exact and Hartree-Fock calculations as a function of a have minima at different values of a. In all cases the exact ground-state energy has a minimum at lower a than for the Hartree-Fock case. The variation in the value of a at the minimum ranged from approximately 12% at low field to 4% at high field. The value of a in the 2D Fock-Darwin case is always slightly smaller than the Hartree-Fock value, as expected because of electron-electron interaction effects. The Fock-Darwin values of a were of the order of 7% less than the Hartree-Fock values for low magnetic fields, dropping to only 2% less at the top of the field range. The exact energy calculated with the Fock-Darwin value of a is therefore consistently lower than that with the Hartree-Fock value; how-

ever, it is difficult to say whether this is generally true without doing calculations for a wide range of devices. The difference in energy between the exact ground states calculated using the Fock-Darwin and Hartree-Fock a values was of the order of 0.0007 meV for 20 T, 0.02 meV for $B=7$ T, but 0.04 meV (0.06%) for $B=0$ T (using up to the second Landau level). These differences become smaller as the number of Landau levels included in the calculation is increased. The errors in the exact energy due to using the Hartree-Fock a are of the same order as from limiting the basis set. We can therefore say that the results presented here are accurate to better than 0.1%.

V. CONCLUSIONS

We have developed a general method for determining the exact states of interacting electrons in a realistic model of a semiconductor nanostructure. The method accounts for the confinement potential of the device, motion perpendicular to the plane of the system, and screening of the electron-electron interaction by metallic electrodes. It is applicable to a wide range of devices and may be generalized to systems that include holes. Energy levels can be determined to better than 0.1% accuracy with reasonable computational cost. A typical run on a HP 735 workstation took 40 min to determine the electrostatic potential, 60 min to find the minimum a, 36 min for the potential matrix elements, 46 min for the look up table for the interaction potential and 260 min for the diagonalization. Not all of these need to be repeated for each run.

We have presented results for the test case of an electrostatically confined quantum dot. In general, the physics of the exact system is well reproduced by the 2D parabolic model but out-of-plane motion and screening increase the fields at which ground-state transitions occur by about 1 T. In addition, out-of-plane motion could allow interaction effects to be seen in optical spectra if the subband spacing was sufficiently small. Finally, the parallel-plate approximation for the screening potential has been shown to be very good for gated nanostructures of the type studied here.

Although the effects we predict are apparently small, there are important consequences for real systems. In particular, small shifts in the magnetic fields at which transitions occur will lead to important corrections to confinement energies deduced from predictions based on the 2D parabolic model. This is because the transition field varies slowly with confinement energy so a small shift in transition field leads to a large shift in a confinement energy deduced by fitting observed fields to a 2D parabolic model.

ACKNOWLEDGMENTS

This work was supported by the UK Engineering and Physical Sciences Research Council.

APPENDIX A: KINETIC ENERGY

The matrix element of the in-plane component of the kinetic energy is the same as for the 2D case, except for the value of a:

$$\begin{aligned}\langle nlm|T_{\|}|n'l'm'\rangle &= -\frac{\hbar^2}{m^*a^2}\delta_{ll'}\delta_{mm'}\{[\tfrac{1}{2}\gamma l-\tfrac{1}{4}(2n+|l|+1)(1+\gamma^2)]\\ &\times\delta_{nn'}+\tfrac{1}{4}(\gamma^2-1)[(n+1)^{1/2}(n+|l|+1)^{1/2}\\ &\times\delta_{n',n+1}+n^{1/2}(n+|l|)^{1/2}\delta_{n',n-1}]\}\end{aligned} \tag{A1}$$

where $\gamma=eBa^2/\hbar$.

The matrix element of the perpendicular component of the kinetic energy is determined by numerically evaluating

$$\langle nlm|T_{\perp}|n'l'm'\rangle=\frac{\hbar^2}{2m^*}\delta_{ll'}\delta_{nn'}\int\chi'_m(z)\chi'_{m'}(z)dz, \tag{A2}$$

where the prime denotes differentiation with respect to the argument. The subband functions and their derivatives were obtained at 2000 points by numerically solving Eq. (8) and a second-order interpolation formula was used to obtain values between these points.

APPENDIX B: CONFINEMENT POTENTIAL

The matrix elements of the confinement potential are given by

$$\begin{aligned}\langle nlm|U|n'l'm'\rangle=\delta_{ll'}\int dz\,d\mathbf{r}\,\chi_m(z)N_{nl}r^{|l|}L_n^{|l|}\left(\frac{r^2}{2a^2}\right)\\ \times e^{-r^2/4a^2}U(\mathbf{r},z)N_{n'l}r^{|l|}L_{n'}^{|l|}\left(\frac{r^2}{2a^2}\right)\\ \times e^{-r^2/4a^2}\chi_{m'}(z).\end{aligned} \tag{B1}$$

To compute this, the integral over z was calculated at every required value of r using 20 000 points. The r integral was then performed for every l and n combination required for the calculation. The integrand was enumerated at 6000 points, spread evenly in r^2 so that more points were concentrated at low r where the integrand was quickly varying. Both integrals were evaluated using a standard third order quadrature rule.[22]

APPENDIX C: COULOMB INTERACTION

We need matrix elements of V for both screened and unscreened interactions and the matrix element of V_I for the screened interaction. In the screened case the matrix element of V is

$$\begin{aligned}\langle ij|V|kl\rangle=\frac{e^2}{4\pi^2\varepsilon}\int\chi_i^*(z)\chi_l(z)\chi_j^*(z')\chi_k(z')p_{ijkl}(q)\\ \times e^{-q^2a^2}f(q,z,z')dz\,dz'dq,\end{aligned} \tag{C1}$$

where $f(q,z,z')$ is given by Eqs. (13) and (14), $p_{ijkl}(q)$ is given by

$$p_{1234}(q)=\sum_{\alpha=0}^{n_1}\sum_{\beta=0}^{n_4}\sum_{\gamma=0}^{n_2}\sum_{\delta=0}^{n_3}\frac{1}{4}A!B!\times\frac{(-1)^{\alpha+\beta+\gamma+\delta}}{\alpha!\beta!\gamma!\delta!}\binom{n_1+|l_1|}{n_1-\alpha}\binom{n_4+|l_4|}{n_4-\beta}\times\binom{n_2+|l_2|}{n_2-\gamma}\binom{n_3+|l_3|}{n_3-\delta}\times\left(\frac{q^2a^2}{2}\right)^{|\eta|}L_A^{|\eta|}\left(\frac{q^2a^2}{2}\right)L_B^{|\eta|}\left(\frac{q^2a^2}{2}\right),$$

and

$$A=\tfrac{1}{2}(\alpha+\beta+\tfrac{1}{2}[|l_1|+|l_4|-|\eta|]),$$

$$B=\tfrac{1}{2}(\gamma+\delta+\tfrac{1}{2}[|l_2|+|l_3|-|\eta|]),$$

$$\eta=l_1-l_4=l_3-l_2.$$

The matrix element of V_I is

$$\langle i|V_I|j\rangle=\frac{e^2}{4\pi\varepsilon}\int_0^\infty dq\int_{-\infty}^{\infty}dz\chi_i(z)\chi_j(z)\left[f(q,z,z)-\frac{1}{2}\right]. \tag{C2}$$

The integrals in Eqs. (C1) and (C2) were evaluated by the trapezium rule with 400 q points, preferentially chosen at low q, and 1000 points for both the z and t integrals.

The matrix elements of the unscreened Coulomb interaction were found with the aid of the relation

$$\frac{1}{\sqrt{r^2+z^2}}=\frac{1}{2\pi}\int\frac{e^{-q|z|}}{q}e^{i\mathbf{q}\cdot\mathbf{r}}d\mathbf{q}, \tag{C3}$$

which leads to the expression

$$\langle n_1l_1m_1n_2l_2m_2|V|n_3l_3m_3n_4l_4m_4\rangle=\frac{(2\pi e)^2}{4\pi\varepsilon}N_{n_1l_1}N_{n_2l_2}N_{n_3l_3}N_{n_4l_4}(\sqrt{2}a)^{|l_1|+|l_2|+|l_3|+|l_4|+4}\times\int_{-\infty}^{\infty}dz\chi_{m_1}^*(z)\chi_{m_4}(z)\int_{-\infty}^{\infty}dt\chi_{m_2}^*(z-t)\chi_{m_3}(z-t)\times\int_0^\infty dqp_{1234}(q)e^{-q|t|}e^{-q^2a^2}. \tag{C4}$$

The behavior of the q integrand is determined by the exponential factors and the size of $|t|$ determines which integration method is most appropriate. For large $|t|$, the $\exp(-q|t|)$ factor is rapidly varying and the Gauss-Laguerre method is used. For small $|t|$, the $\exp(-q^2a^2)$ factor is the most influential and a simple quadrature rule is most appropriate. In practice, the Gauss-Laguerre method with 60 points was used for $|t|\geqslant 2a$ and a standard quadrature rule[22] with 5000 points for $|t|<2a$. The z and t integrals were done with the same rule, each with 1000 points.

[1] P.A. Maksym and T. Chakraborty, Phys. Rev. Lett. **65**, 108 (1990).

[2] N.F. Johnson and M.C. Payne, Phys. Rev. Lett. **67**, 1157 (1991).

[3] A. Kumar, S.E. Laux, and F. Stern, Phys. Rev. B **42**, 5166 (1990).

[4] L.D. Hallam, N.A. Bruce, and P.A. Maksym, Surf. Sci. **361/362**, 648 (1996).

[5] T.H. Oosterkamp, J.W. Jansen, L.P. Kouwenhoven, D.G. Austing, T. Honda, and S. Tarucha, Phys. Rev. Lett. **82**, 2931 (1999).

[6] R.C. Ashoori, H. L. Störmer, J. S. Weiner, L. N. Pfeiffer, K. W. Baldwin, and K. W. West, Phys. Rev. Lett. **71**, 613 (1993).

[7] D. Heitmann and J.P. Kotthaus, Phys. Today **46(6)**, 56 (1993); M.A. Reed, J. N. Randall, R. J. Aggarwal, R. J. Matyi, T. M. Moore, and A. E. Wetsel, Phys. Rev. Lett. **60**, 535 (1988); K. Nomoto, T. Suzuki, K. Taira, and I. Hase, Jpn. J. Appl. Phys. **33**, L1142 (1994).

[8] J. Tulkki and A. Heinämäki, Phys. Rev. B **52**, 8239 (1995).

[9] M. Grundmann, O. Stier, and D. Bimberg, Phys. Rev. B **52**, 11 969 (1995).

[10] R.C. Ashoori, H. L. Störmer, J. S. Weiner, L. N. Pfeiffer, S. J. Pearton, K. W. Baldwin, and K. W. West, Phys. Rev. Lett. **68**, 3088 (1992); S.A. Rishton, Y. H. Lee, K. R. Milkove, J. M. Hong, V. Boegli, M. Defranza, U. Sivan, and D. P. Kern, J. Vac. Sci. Technol. B **11**, 2607 (1993); A.K. Geim, P. C. Main, N. Lascala, L. Eaves, T. J. Foster, P. M. Beton, J. W. Sakai, F. W. Sheard, M. Henini, G. Hill, and M. A. Pate, Phys. Rev. Lett. **72**, 2061 (1994); J. Smoliner, W. Demmerle, E. Gornik, G. Bohm, and G. Weimann, Semicond. Sci. Technol. **9**, 1925 (1994); K. Nomoto, T. Suzuki, K. Taira, and I. Hase, Jpn. J. Appl. Phys. **33**, L1142 (1994); D.G. Austing, T. Honda, Y. Tokura, and S. Tarucha, *ibid.* **34**, 1320 (1995); G. Biese, C. Schuller, K. Keller, C. Steinebach, D. Meitmann, P. Grambow, and K. Eberl, Phys. Rev. B **53**, 9565 (1996).

[11] K. Lier and R.R. Gerhardts, Phys. Rev. B **48**, 14 416 (1993).

[12] L.D. Hallam, J. Weis, and P.A. Maksym, Phys. Rev. B **53**, 1452 (1996).

[13] V. Fock, Z. Phys. **47**, 446 (1928); C.G. Darwin, Proc. Cambridge Philos. Soc. **27**, 86 (1930).

[14] P.A. Maksym and N.A. Bruce, Physica E (Amsterdam) **1**, 211 (1997).

[15] P.A. Maksym, Phys. Rev. B **53**, 10 871 (1996).

[16] S. Tarucha, D.G. Austing, T. Honda, R.J. Vanderhage, and L.P. Kouvenhoven, Phys. Rev. Lett. **77**, 3613 (1996).

[17] M. Eto, J. Phys. Soc. Jpn. **66**, 2244 (1997).

[18] L. Brey, N.F. Johnson, and B.I. Halperin, Phys. Rev. B **40**, 10 647 (1989).

[19] D.A. Broido, K. Kempa, and P. Bakshi, Phys. Rev. B **42**, 11 400 (1990), V. Gudmunsson and R. Gerhardts, *ibid.* **43**, 12 098 (1991); D. Pfannkuche and R. Gerhardts, *ibid.* **44**, 13 132 (1991).

[20] A. Corney, *Atomic and laser spectroscopy* (Clarendon Press, Oxford 1977), p. 279.

[21] P.A. Maksym and T. Chakraborty, Phys. Rev. B **45**, 1947 (1992).

[22] P.E. Gill and G.F. Miller, Comput. J. (UK) **15**, 80 (1972). The method is implemented in the NAG numerical library.